Modeling longitudinal wave propagation in nonlinear viscoelastic solids with softening

Harold Berjamin, Bruno Lombard, Guillaume Chiavassa, Nicolas Favrie

Modeling longitudinal wave propagation in nonlinear viscoelastic solids with softening

Harold Berjamin[a], Bruno Lombard[a,*], Guillaume Chiavassa[b], Nicolas Favrie[c]

[a] *Aix-Marseille Univ, CNRS, Centrale Marseille, LMA, Marseille, France*
[b] *Centrale Marseille, CNRS, Aix-Marseille Univ, M2P2 UMR 7340, 13451 Marseille Cedex 20, France*
[c] *Aix-Marseille Univ, UMR CNRS 7343, IUSTI, Polytech Marseille, 13453 Marseille Cedex 13, France*

Abstract

A model for longitudinal wave propagation in rocks and concrete is presented. Such materials are known to soften under a dynamic loading, i.e. the speed of sound diminishes with forcing amplitudes. Also known as slow dynamics, the softening of the material is not instantaneous. Based on continuum mechanics with internal variables of state, a new formulation is proposed, which accounts for nonlinear Zener viscoelasticity and softening. A finite-volume method using Roe linearization is developed for the system of partial differential equations so-obtained. The method is used to carry out resonance simulations, and its performance is assessed in the linear viscoelastic case. Qualitative agreement with experimental results of nonlinear ultrasound spectroscopy (NRUS) and dynamic acousto-elastic testing (DAET) is obtained.

Keywords: Nonlinear acoustics, softening, viscoelasticity, numerical methods
PACS: 43.25.+y, 43.25.Dc, 02.70.Bf

1. Introduction

Longitudinal vibrations of rocks and concrete highlight features which cannot be reproduced by standard elastodynamics [1]. First, in nonlinear resonance ultrasound spectroscopy (NRUS), a frequency-shift of the resonance peaks with the amplitude of forcing is observed [2, 3]. This feature reveals the highly nonlinear behavior of such material. Second, in dynamic acousto-elastic testing (DAET) [4, 5], a decrease of the sound speed over a time scale larger than the period of the dynamic loading is observed (*softening*), which highlights the phenomenon of *slow dynamics*. When the excitation is stopped, the sound speed recovers gradually its initial value (*recovery*). Third and last, hysteresis curves are obtained when the speed of sound is represented with respect to the axial strain. All these phenomena are accentuated when the forcing amplitude is increased.

Several models can be found in the literature to describe these phenomena (see e.g. [6–8]). The approach proposed by Vakhnenko et al. in their *soft-ratchet* model [9, 10] consists in adding a variable g to describe the softening of the material. Also, an evolution equation for g is provided, and a relaxation time is included. A similar model with refinements was proposed by

*Corresponding author
Email address: lombard@lma.cnrs-mrs.fr (Bruno Lombard)

Lyakhovsky and coauthors in a series of papers [11, 12], with application to resonance experiments [13]. Recently, a 3D model of continuum [14] has been developed by the authors in the framework of continuum thermodynamics with internal variables of state [15, 16]. This model generalizes the soft-ratchet model to 3D geometries and fixes thermodynamical issues. The first goal of the present paper is to show how viscoelastic attenuation of Zener type can be accounted for, by adding a set of relaxation equations. This modeling step is necessary to reproduce the vibrations of real materials.

The equations of motion write as a system of conservation laws with relaxation terms. Thus, the numerical techniques for nonlinear hyperbolic systems apply [17–19]. The second goal of the present paper is then to derive a finite-volume method based on the Roe linearization by computing an adequate Roe matrix. Second-order accuracy is obtained by using Strang splitting, where an adaptive Rosenbrock method is used for the relaxation part. The resulting scheme is well-suited for nonlinear wave propagation, in the case of smooth acoustic waves.

The article is organized as follows. The physical model is proposed in section 2. Then, the numerical method is developed (section 3). In particular, the construction of a Roe matrix is detailed. In section 4, several numerical experiments are carried out. Firstly, resonance curves are estimated numerically. Secondly, dynamic acousto-elasticity experiments are reproduced. The results are in qualitative agreement with experimental observations.

Appendix A describes the optimization procedure to determine the parameters of the Zener model. Appendix B gives details about the construction of the Roe matrix.

2. Physical modeling

Let us consider a solid continuum in the Lagrangian representation of motion, which length L along the x-axis is very large compared to its other dimensions. No heat transfer occurs in the material, and self-gravitation is neglected. Only longitudinal vibrations are considered, and the displacement field is described by its component $u(x,t)$ along the x-axis. On one hand, kinematics reads

$$\frac{\partial \varepsilon}{\partial t} = \frac{\partial v}{\partial x}\,, \tag{1}$$

where $\varepsilon = \partial u/\partial x > -1$ denotes the strain, and $v = \partial u/\partial t$ denotes the particle velocity. On the other hand, the conservation of momentum writes

$$\rho_0 \frac{\partial v}{\partial t} = \frac{\partial \sigma}{\partial x}\,, \tag{2}$$

where ρ_0 is the density in the reference (undeformed) configuration. According to the conservation of mass, the density ρ in the deformed configuration satisfies $\rho_0/\rho = 1 + \varepsilon$. The expression of the stress σ in (2) will be specified later on.

2.1. Nonlinear viscoelasticity

Experimental evidence shows that elastic models are not sufficient to model vibrations in concrete and geomaterials. In particular, resonance experiments demonstrate the need of attenuation to describe accurately wave propagation in real media [1–3]. In the framework of linear elasticity, several rheological models based on a combination of springs and dashpots can be found in the literature. The standard linear solid, also known as generalized Zener or Maxwell

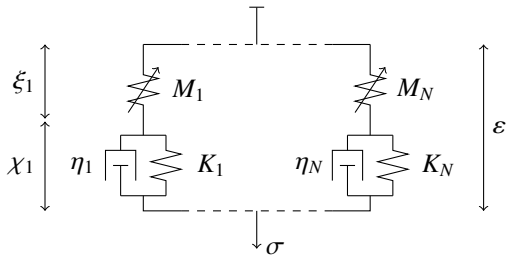

Figure 1: Rheological model of a nonlinear generalized Zener material.

body, is commonly used for the description of seismic wave propagation [20–22]. It consists in the combination of N elementary Zener mechanisms with elastic constants $M_\ell > 0$, $K_\ell > 0$ and damping constants $\eta_\ell > 0$, where $\ell = 1, \dots, N$. Here, a generalization of the standard linear solid to nonlinear constitutive laws proposed in [10] is used. The corresponding schematic representation in terms of springs and dashpots is given in figure 1. When the springs with constant M_ℓ are linear springs, the standard linear solid model is recovered. Furthermore, inviscid nonlinear elasticity is recovered when the viscous effects are null, in the sense that $\eta_\ell \to +\infty$ for $\ell = 1, \dots, N$.

The parameters of the model M_ℓ, K_ℓ, η_ℓ are deduced from the quality factor Q of the material over a frequency range of interest [10, 22]. To do so, the relaxation times $\tau_{\sigma\ell}$, $\tau_{\varepsilon\ell}$ and the relaxed elastic modulus M_{rel} are introduced:

$$\tau_{\sigma\ell} = \frac{\eta_\ell}{M_\ell + K_\ell}\,, \qquad \tau_{\varepsilon\ell} = \frac{\eta_\ell}{K_\ell}\,, \qquad \frac{M_{\text{rel}}}{N} = \frac{M_\ell K_\ell}{M_\ell + K_\ell}\,. \tag{3}$$

In the following numerical experiments, $N = 5$ Zener mechanisms are used, and the quality factor is optimized over the frequency range $[f_{\min}, f_{\max}] = [1, 100]$ kHz towards the value $Q = 20$. The relaxation times $\tau_{\sigma\ell}$, $\tau_{\varepsilon\ell}$ are deduced from a nonlinear optimization procedure described briefly in Appendix A.

In the case of nonlinear Zener materials [10], the linear springs with constant M_ℓ are replaced by nonlinear springs (figure 1). Their state of deformation is described by the variables ξ_ℓ, and their strain energy density W_ℓ is expressed by using a suitable strain energy density function. For example, W_ℓ may be expressed as a polynomial function of the strain [14]

$$W_\ell : \xi_\ell \mapsto \left(\frac{1}{2} - \frac{\beta}{3}\xi_\ell - \frac{\delta}{4}{\xi_\ell}^2\right) M_\ell\, {\xi_\ell}^2\,, \tag{4}$$

where the dimensionless parameters β and δ are high-order elastic constants. The polynomial expression of the strain energy density (4) is widely used to describe nonlinear elastic materials in the community of nondestructive evaluation. The strain energy function (4) amounts to Hooke's law $W_\ell = \frac{1}{2} M_\ell\, {\xi_\ell}^2$ in the case of small strains $\xi_\ell \to 0$, which is also recovered by setting $\beta = 0$ and $\delta = 0$ in (4).

In counterpart, the parts with spring constant K_ℓ and damping constant η_ℓ are still considered as linear, but other choices are also suitable. Their state of deformation is described by the variables $\chi_\ell = \varepsilon - \xi_\ell$, so that the strain energy density in each mechanism is $\frac{1}{2} K_\ell\, {\chi_\ell}^2$. Finally, the

total strain energy W in the material is the sum of the strain energies in all the springs:

$$W = \sum_{\ell=1}^{N} W_\ell(\varepsilon - \chi_\ell) + \frac{1}{2} K_\ell {\chi_\ell}^2 . \tag{5}$$

According to the diagram in figure 1, the stress σ_ℓ in the ℓth Zener mechanism is expressed by

$$\sigma_\ell = W'_\ell(\varepsilon - \chi_\ell) , \tag{6}$$

$$= K_\ell \chi_\ell + \eta_\ell \frac{\partial \chi_\ell}{\partial t} , \tag{7}$$

where W'_ℓ is the derivative of the function W_ℓ. Combining (6) and (7), the evolution equations

$$\frac{\partial \chi_\ell}{\partial t} = \frac{1}{\eta_\ell} \left(W'_\ell(\varepsilon - \chi_\ell) - K_\ell \chi_\ell \right) \tag{8}$$

are obtained. The relation $\sigma = \sum_{\ell=1}^{N} \sigma_\ell$ and (6) lead to the constitutive law

$$\sigma = \sum_{\ell=1}^{N} W'_\ell(\varepsilon - \chi_\ell) . \tag{9}$$

2.2. Softening

To describe the softening of the nonlinear viscoelastic material, we introduce a scalar variable g, which value in $[0, 1[$ modifies the stiffness of the material. This variable is modified along the time following an evolution equation. Similarly to [14], the derivation of a softening model is based on continuum thermodynamics with internal variables [15, 16]. As usual in acoustics, the process is assumed adiabatic. The first principle of thermodynamics introduces the internal energy e per unit of initial volume. The conservation of total energy writes

$$\dot{e} = \sigma \dot{\varepsilon} , \tag{10}$$

where the dot denotes the material time-derivative $\partial/\partial t$. The second principle of thermodynamics reads

$$\rho_0 \dot{s} \geq 0 , \tag{11}$$

where s is the specific entropy. The system is described by the variables of state $\{\varepsilon, s, \chi_1, \ldots, \chi_\ell, g\}$, leading to the Gibbs identity

$$\dot{e} = \rho_0 T \dot{s} + \frac{\partial e}{\partial \varepsilon} \dot{\varepsilon} + \frac{\partial e}{\partial \boldsymbol{p}} \cdot \dot{\boldsymbol{p}} , \tag{12}$$

where $T = {\rho_0}^{-1} \partial e / \partial s > 0$ is the absolute temperature. The variable $\boldsymbol{p} = (\chi_1, \ldots, \chi_N, g)^\top$ is a vector of internal variables, which evolution $\dot{\boldsymbol{p}}$ depends only on the state of the system. Combining (10), (11) and (12), the Clausius-Duhem inequality is obtained:

$$\mathcal{D} = \left(\sigma - \frac{\partial e}{\partial \varepsilon} \right) \dot{\varepsilon} - \frac{\partial e}{\partial \boldsymbol{p}} \cdot \dot{\boldsymbol{p}} \geq 0 , \tag{13}$$

for all state $\{\varepsilon, \boldsymbol{p}\}$ and all evolution $\dot{\varepsilon}$. The left-hand term in (13) is the dissipation $\mathcal{D}$ per initial volume of material (W m^{-3}).

Analogously to the Ogden-Roxburgh model of filled rubber [14, 23], we assume an internal energy per unit of initial volume of the following form:

$$e = (1 - g)\, W + \phi(g)\,, \tag{14}$$

with W given in (5). The first term in (14) is the strain energy. Similarly to models of isotropic damage [24], the softening of the material is expressed by multiplying the strain energy W of the undamaged material by $1 - g$. Hence, the material is undamaged when $g = 0$, and completely destroyed when $g \to 1$. The second term $\phi(g)$ is a storage energy. A suitable expression of the storage energy is

$$\phi(g) = -\frac{1}{2}\gamma \ln\left(1 - g^2\right), \tag{15}$$

where $\gamma > 0$ is an energy per unit volume, but other choices are possible. As discussed in [14], this expression is chosen such that equilibrium points are unique, the value $g = 0$ is an equilibrium point, and g is bounded by 1. For small values of g, the storage energy is $\phi(g) \simeq \frac{1}{2}\gamma g^2$.

Both the internal energy e and the stress σ are state functions. Thus, the Clausius-Duhem inequality (13) rewrites as $A(\varepsilon, \boldsymbol{p})\, \dot{\varepsilon} + B(\varepsilon, \boldsymbol{p}) \geq 0$, where $A = \sigma - \partial e/\partial \varepsilon$ and $B = -\partial e/\partial \boldsymbol{p} \cdot \dot{\boldsymbol{p}}$. To ensure a positive dissipation for all $\dot{\varepsilon}$, one must have $A = 0$ and $B \geq 0$, i.e.

$$\sigma = \frac{\partial e}{\partial \varepsilon} \qquad \text{and} \qquad -\frac{\partial e}{\partial \boldsymbol{p}} \cdot \dot{\boldsymbol{p}} \geq 0\,. \tag{16}$$

The first condition in (16) leads to the constitutive law

$$\sigma = (1 - g) \sum_{\ell=1}^{N} W_\ell'(\varepsilon - \chi_\ell)\,. \tag{17}$$

The expression of the stress is the same as in the viscoelastic case (9), but multiplied by $1 - g$. The second condition in (16) yields the possible choice

$$\dot{\boldsymbol{p}} = -\operatorname{diag}\left(\frac{1}{(1 - g)\,\eta_1}, \ldots, \frac{1}{(1 - g)\,\eta_N}, \frac{1}{\alpha}\right) \frac{\partial e}{\partial \boldsymbol{p}}\,, \tag{18}$$

where $\alpha > 0$ is a constant expressed in J m^{-3} s. Thus, the evolution equations of viscoelasticity (8) are unchanged, and the evolution of the softening variable g is governed by

$$\alpha \dot{g} = W - \phi'(g)\,, \tag{19}$$

where ϕ' is the derivative of the storage energy (15) and W is given in (5). Finally, the dissipation per unit of initial volume is $B = -\partial e/\partial \boldsymbol{p} \cdot \dot{\boldsymbol{p}}$, i.e.

$$\mathcal{D} = \alpha \dot{g}^2 + (1 - g) \sum_{\ell=1}^{N} \eta_\ell\, (\dot{\chi}_\ell)^2\,, \tag{20}$$

which is positive. If $\alpha \to +\infty$, then no softening occurs: the viscoelastic case from section 2.1 is recovered. Conversely, if $\alpha \to 0$, the material softens instantaneously. As shown in [14], the constant

$$\tau_g = \frac{\alpha}{\gamma} \tag{21}$$

is the relaxation time of the slow dynamics.

To summarize, the equations of motion are (1), (2) with the constitutive law (17), and the evolution equations (18). For convenience, we use now the relation $\chi_\ell = \varepsilon - \xi_\ell$ to eliminate the variables χ_ℓ. The evolution of the variables ξ_ℓ is governed by $\dot{\xi}_\ell = \dot{\varepsilon} - \dot{\chi}_\ell$, where $\dot{\varepsilon}$ and $\dot{\chi}_\ell$ are specified in (1) and (8), respectively. Thus, a system of $N + 3$ partial differential equations in space and time is obtained,

$$\begin{cases} \dfrac{\partial \varepsilon}{\partial t} = \dfrac{\partial v}{\partial x}\,, \\ \rho_0 \dfrac{\partial v}{\partial t} = \dfrac{\partial}{\partial x}\sigma \qquad \text{with} \qquad \sigma = (1-g)\displaystyle\sum_{\ell=1}^{N} W_\ell'(\xi_\ell)\,, \\ \dfrac{\partial \xi_\ell}{\partial t} = \dfrac{\partial v}{\partial x} + \dfrac{1}{\eta_\ell}\Big(K_\ell\,(\varepsilon - \xi_\ell) - W_\ell'(\xi_\ell)\Big)\,, \qquad \ell = 1, \dots, N\,, \\ \alpha \dfrac{\partial g}{\partial t} = \left(\displaystyle\sum_{\ell=1}^{N} W_\ell(\xi_\ell) + \frac{1}{2}K_\ell\,(\varepsilon - \xi_\ell)^2\right) - \phi'(g)\,, \end{cases} \tag{22}$$

with $N + 3$ unknowns. The system (22) rewrites as a system of conservation laws with relaxation

$$\frac{\partial}{\partial t}\boldsymbol{U} + \frac{\partial}{\partial x}\boldsymbol{F}(\boldsymbol{U}) = \boldsymbol{R}(\boldsymbol{U})\,, \tag{23}$$

where $\boldsymbol{U} = (\varepsilon, v, \xi_1, \dots, \xi_N, g)^\top$ is the vector of unknowns. The physical flux $\boldsymbol{F}(\boldsymbol{U})$ and the relaxation function $\boldsymbol{R}(\boldsymbol{U})$ are

$$\begin{aligned} \boldsymbol{F}(\boldsymbol{U}) &= -\left(v, \frac{\sigma}{\rho_0}, v, \dots, v, 0\right)^\top, \\ \boldsymbol{R}(\boldsymbol{U}) &= \left(0, 0, \frac{K_1\,(\varepsilon - \xi_1) - W_1'(\xi_1)}{\eta_1}, \dots, \frac{K_N\,(\varepsilon - \xi_N) - W_N'(\xi_N)}{\eta_\ell}, \frac{W - \phi'(g)}{\alpha}\right)^\top, \end{aligned} \tag{24}$$

where the stress σ is deduced from the constitutive law (17), the strain energy W is defined in (5), and the storage energy ϕ is given in (15).

2.3. Properties

2.3.1. Mathematical properties

Hyperbolic system of conservation laws. Some properties of the system (23) without relaxation, i.e. $\boldsymbol{R}(\boldsymbol{U}) = \boldsymbol{0}$, are listed below without proof. Interested readers are referred to standard textbooks about hyperbolic systems of conservation laws [17, 18, 25]. Details about the analysis hereinafter can be found in [26].

The Jacobian matrix $\boldsymbol{F}'(\boldsymbol{U})$ of the physical flux has the eigenvalues $\{-c(\boldsymbol{U}), 0, \dots, 0, +c(\boldsymbol{U})\}$, where the speed of sound $c(\boldsymbol{U})$ satisfies

$$\rho_0\, c(\boldsymbol{U})^2 = (1-g)\sum_{\ell=1}^{N} W_\ell''(\xi_\ell)\,. \tag{25}$$

The hyperbolicity of the system (23) amounts to the fact that $c(\boldsymbol{U})$ is real and strictly positive. A sufficient condition is that g belongs to $[0, 1[$, and that ξ_ℓ satisfies $W_\ell''(\xi_\ell) > 0$ for all ℓ. In the

Table 1: Physical parameters.

ρ_0 (kg/m^3)	M_0 (GPa)	β	δ	Q	γ (J/m^3)	α (J/m^3.s)
2.6×10^3	10	200	10^8	20	1.0	10^{-3}

case of the polynomial law (4), $W_\ell''(\xi_\ell)$ is positive provided that

$$\xi_\ell \in \left]\frac{1}{\beta - \sqrt{\beta^2 + 3\delta}}, \frac{1}{\beta + \sqrt{\beta^2 + 3\delta}}\right[. \tag{26}$$

If $\beta = \delta = 0$, the stress-strain relationship $\xi_\ell \mapsto W_\ell'(\xi_\ell)$ deduced from the polynomial law (4) is linear, and all $N + 3$ characteristic fields are linearly degenerate. Otherwise, there are $N + 1$ linearly degenerate characteristic fields, corresponding to zero eigenvalues. If $\beta > 0$ and $\delta = 0$, then the stress-strain relationship is concave. The two remaining characteristic fields with eigenvalues $\pm c$ are genuinely nonlinear. If $\delta \neq 0$, the stress-strain relationship is neither convex nor concave. Indeed, the constitutive law has an inflexion point at the strain $\varepsilon_0 = -\beta/(3\delta)$. Then, the two characteristic fields with eigenvalues $\pm c$ are neither genuinely nonlinear nor linearly degenerate (nongenuinely nonlinear).

Relaxation spectrum. Now, we examine the spectrum of the relaxation function $\boldsymbol{R}$ in (24). In the small parameter limit, $W_\ell(\xi_\ell) \simeq \frac{1}{2} M_\ell {\xi_\ell}^2$ amounts to Hooke's law and $\phi(g) \simeq \frac{1}{2}\gamma g^2$. The eigenvalues of the Jacobian matrix $\boldsymbol{R}'(\boldsymbol{U})$ are then $\{-1/\tau_{\sigma N}, \ldots, -1/\tau_{\sigma 1}, -1/\tau_g, 0, 0\}$, where the relaxation times are defined by (3) and (21). As discussed in the Appendix A, the relaxation times $\tau_{\sigma\ell}$ belong to a frequency range $[f_{\min}, f_{\max}]$ surrounding the excitation frequency. If the relaxation times $\tau_{\sigma\ell}$ are sorted in descending order, then $f_{\min} \approx 1/\tau_{\sigma 1} < 1/\tau_{\sigma N} \approx f_{\max}$. Using the numerical values in table 1, one shows that the characteristic frequency $1/\tau_g$ of the slow dynamics is smaller than the exciting frequency. Therefore, the spectral radius of $\boldsymbol{R}'(\boldsymbol{U})$ is equal to $1/\tau_{\sigma N}$.

2.3.2. Qualitative properties

Sinusoidal strain forcing. To illustrate the decrease of the elastic modulus, we consider that a sinusoidal strain with frequency $f_c = 2$ kHz and amplitude $V \approx 10^{-6}$ is applied locally to the material. The evolution equations (8) and (19) for the variables $\chi_1, \ldots, \chi_N$ and g are integrated numerically, with physical parameters given in the tables 1 and A.3. The Matlab solver "ode15s" for stiff differential equations is used with at least 80 points per period at the frequency f_c. The effective elastic modulus is $M = \rho_0\, c^2$, where c is the speed of sound (25). In figure 2-(a), the time evolution of its relative variation

$$\frac{\Delta M}{M} = \rho_0\, c^2 \Big/ \left(\sum_{\ell=1}^{N} M_\ell\right) - 1 \tag{27}$$

is represented for increasing strain amplitudes V. A diminution of the effective elastic modulus is observed, until a steady state is reached. Figure 2-(b) represents the relative variation of the effective elastic modulus with respect to the strain in steady state ($t \gg \tau_g$). Hysteresis curves are obtained, which size increases with the strain amplitude. In figure 2-(c), the hysteresis in the

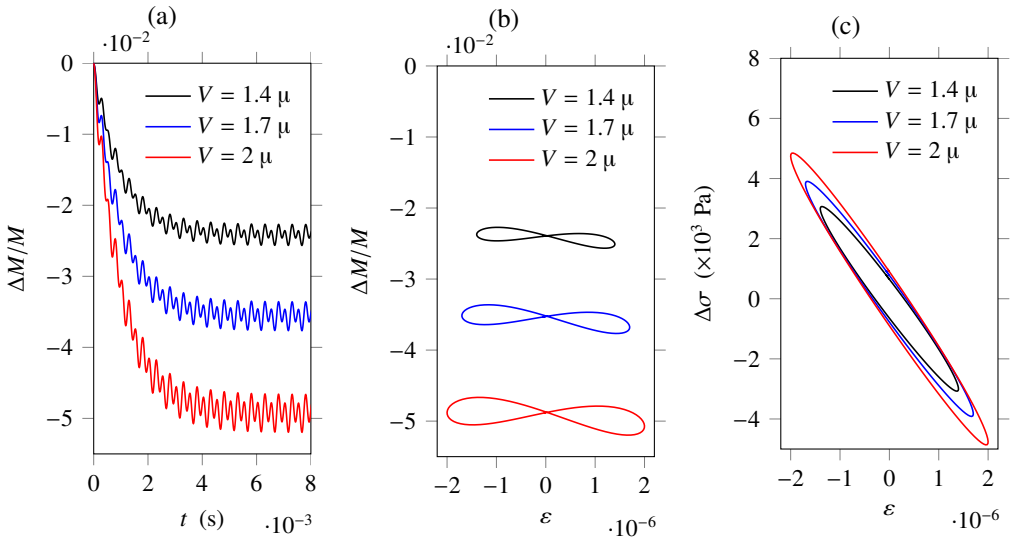

Figure 2: Softening in the case of a sinusoidal strain forcing $\varepsilon = V \sin(2\pi f_c t)$. (a) Time evolution of the relative variation $\Delta M/M$ of the effective elastic modulus (27). (b) Hysteresis curves $\Delta M/M$ versus ε in steady state ($t \gg \tau_g$); (c) effect of hysteresis on the stress-strain relationship. The stress variation $\Delta\sigma$ defined in (28) is represented with respect to ε.

stress-strain relationship (17) is represented. Here, the variation of the stress

$$\Delta\sigma = \sigma - \sum_{\ell=1}^{N} M_\ell \varepsilon \tag{28}$$

is represented with respect to the strain. The hysteresis curves have the shape of ellipses. The slope of their major axis diminishes with increasing strain amplitudes, which illustrates the softening of the material.

Strain step. Now, we consider that a strain step of amplitude ε is applied locally to the material. The variable χ_ℓ evolves in time towards its equilibrium value χ_ℓ^*, and the corresponding relaxation time is $\tau_{\sigma\ell}$. The equilibrium value of χ_ℓ is implicitly defined as a function of ε by the relation

$$W_\ell'\left(\varepsilon - \chi_\ell^*\right) = K_\ell \chi_\ell^*\,, \tag{29}$$

i.e. $\chi_\ell^* = \frac{M_\ell}{M_\ell + K_\ell}\varepsilon$ in the case of Hooke's law ($\beta = 0$ and $\delta = 0$ in (4)). The variable g evolves in time towards its equilibrium value

$$g^* = (\phi')^{-1}(W^*)\,, \tag{30}$$

where W^* is the strain energy (5) at equilibrium. Assuming the separation of time scales $\tau_{\sigma 1} \ll \tau_g$, the corresponding relaxation time is τ_g (21). With the logarithmic expression (15) of the storage energy, the equilibrium value (30) is

$$g^* = \frac{2W^*}{\gamma + \sqrt{\gamma^2 + 4W^*}}\,, \tag{31}$$

which is bounded by 1 for all $W^* \geq 0$. In the case of Hooke's law, the strain energy at equilibrium $W^* = \frac{1}{2} M_{\text{rel}}\, \varepsilon^2$ is deduced from the expression of χ_ℓ^* and from the definition (3) of M_{rel}. Thus,

$$g^* = \frac{M_{\text{rel}}\, \varepsilon^2}{\gamma + \sqrt{\gamma^2 + 2 M_{\text{rel}}\, \varepsilon^2}} \underset{(\varepsilon \to 0)}{\simeq} \frac{M_{\text{rel}}\, \varepsilon^2}{2\gamma}\,. \tag{32}$$

Similar results were obtained in the elastic case [14].

3. Numerical resolution

3.1. Numerical strategy

We consider a finite domain $[0, L]$. It is discretized using a regular grid in space with mesh size Δx. The abscissas of the nodes are $x_i = i\,\Delta x$, where $0 \leq i \leq N_x$ and the number of nodes is $N_x = L/\Delta x$. A variable time step $\Delta t = t_{n+1} - t_n$ is introduced. Therefore, $\boldsymbol{U}(x_i, t_n)$ is the solution to (23) at the ith grid node and at the nth time step. Numerical approximations of the solution are denoted by $\boldsymbol{U}_i^n \simeq \boldsymbol{U}(x_i, t_n)$.

As discussed in [10], an efficient and flexible numerical strategy results from splitting the system (23) in a propagation part (or hyperbolic part)

$$\frac{\partial}{\partial t}\boldsymbol{U} + \frac{\partial}{\partial x}\boldsymbol{F}(\boldsymbol{U}) = \boldsymbol{0} \tag{33}$$

and a relaxation part

$$\frac{\partial}{\partial t}\boldsymbol{U} = \boldsymbol{R}(\boldsymbol{U})\,. \tag{34}$$

The discrete operators corresponding to the discretization of (33) and (34) are denoted $\boldsymbol{H}_a$ and $\boldsymbol{H}_b$, respectively. Numerically, both parts are solved successively at each time step, with dedicated numerical methods. Here, a second-order accurate Strang splitting scheme

$$\begin{cases} \boldsymbol{U}_i^{(1)} = \boldsymbol{H}_b(\Delta t/2)\,[\boldsymbol{U}_i^n] \\ \boldsymbol{U}_i^{(2)} = \boldsymbol{H}_a(\Delta t)\left[\boldsymbol{U}_i^{(1)}\right] \\ \boldsymbol{U}_i^{n+1} = \boldsymbol{H}_b(\Delta t/2)\left[\boldsymbol{U}_i^{(2)}\right] \end{cases} \tag{35}$$

is used. As described in the next subsections, both $\boldsymbol{H}_a$ and $\boldsymbol{H}_b$ are fourth-order accurate operators. The operator $\boldsymbol{H}_a$ is stable under the CFL condition (38), whereas the operator $\boldsymbol{H}_b$ is made unconditionally stable using an adaptive Rosenbrock method. Thus, the coupled scheme (35) is stable under the CFL condition. A second-order error is introduced by the splitting [18], which penalizes the fourth-order accuracy of each operator. Nevertheless, the global accuracy observed practically is much larger than with second-order schemes. This choice reduces significantly numerical diffusion, which is crucial in the simulation of resonance experiments.

3.2. Propagation part

The numerical resolution of nonlinear systems of conservation laws (33) is usually performed using nonlinear conservative schemes such as finite-volume schemes with flux limiters, MUSCL or WENO schemes [18, 27]. Such methods are designed to capture nonsmooth solutions without introducing spurious oscillations. However, the presence of viscoelasticity prevents the occurence of shocks. Therefore, this approach would be either too expensive from a computational point of view, or it would introduce to much numerical diffusion. Here, a fourth-order conservative ADER scheme [28, 29], well-suited to smooth solutions, is preferred.

Table 2: Coefficients Υ_{jk} in the numerical flux of the ADER scheme (37).

j	k			
	0	1	2	3
$i-1$	$-1/12$	$-1/24$	$1/12$	$1/24$
i	$7/12$	$5/8$	$-1/12$	$-1/8$
$i+1$	$7/12$	$-5/8$	$-1/12$	$1/8$
$i+2$	$-1/12$	$1/24$	$1/12$	$-1/24$

ADER scheme. The homogeneous system of conservation laws (33) is integrated numerically in space and time according to

$$\boldsymbol{H}_a(\Delta t)\,[\boldsymbol{U}_i^n] = \boldsymbol{U}_i^n - \frac{\Delta t}{\Delta x}\left(\boldsymbol{F}_{i+1/2}^n - \boldsymbol{F}_{i-1/2}^n\right), \tag{36}$$

where $\boldsymbol{F}_{i+1/2}^n$ is the numerical flux. The physical flux $\boldsymbol{F}(\boldsymbol{U})$ is approximated locally by the linear flux $\boldsymbol{A}_{i+1/2}\,\boldsymbol{U}$ at each time step, where $\boldsymbol{A}_{i+1/2}$ approximates the Jacobian $\boldsymbol{F}'(\boldsymbol{U})$ at the midpoint of $[x_i, x_{i+1}]$ and the time t_n. The numerical flux of the ADER scheme is then obtained similarly to the flux of the Lax-Wendroff scheme for nonlinear systems (see section 12.2 of [30]). Thus,

$$\boldsymbol{F}_{i+1/2}^n = \sum_{j=i-1}^{i+2}\sum_{k=0}^{3}\Upsilon_{jk}\left(\frac{\Delta t}{\Delta x}\boldsymbol{A}_{i+1/2}\right)^k \boldsymbol{F}(\boldsymbol{U}_j^n)\,, \tag{37}$$

where the coefficients Υ_{jk} are given in table 2.

In practice, the numerical scheme (36) with the numerical flux (37) is stable under the classical CFL condition

$$\kappa = c_{\max}^n\,\frac{\Delta t}{\Delta x} \le 1\,, \tag{38}$$

where κ is the Courant number and $c_{\max}^n$ denotes the maximum sound speed (25) that is encountered at time t_n. If the stress-strain relationship $\xi_\ell \mapsto W_\ell'(\xi_\ell)$ is convex or concave, then $c_{\max}^n = \max_i c(\boldsymbol{U}_i^n)$. Otherwise, larger sound speeds may be reached between grid nodes (see e.g. section 16.1 in [18]). The more general expression is

$$\rho_0\,(c_{\max}^n)^2 = \max_{0\le i<N_x}\left\{(1-\min\{g_i^n, g_{i+1}^n\})\sum_{\ell=1}^{N}\max_{\xi_\ell\in(\Gamma_\ell)_i} W_\ell''(\xi_\ell)\right\}, \tag{39}$$

where $(\Gamma_\ell)_i$ is the interval with bounds $(\xi_\ell)_i^n$ and $(\xi_\ell)_{i+1}^n$.

Roe linearization. Here, the matrix $\boldsymbol{A}_{i+1/2}$ is obtained by Roe linearization. The Roe matrix is defined by the following statements [18]:

1. the matrix $\boldsymbol{A}_{i+1/2}$ is diagonalizable with real eigenvalues;
2. the discrete Rankine-Hugoniot condition holds for all $\boldsymbol{U}_i^n$ and $\boldsymbol{U}_{i+1}^n$:

$$\boldsymbol{A}_{i+1/2}\,(\boldsymbol{U}_{i+1}^n - \boldsymbol{U}_i^n) = \boldsymbol{F}(\boldsymbol{U}_{i+1}^n) - \boldsymbol{F}(\boldsymbol{U}_i^n)\,;$$

3. the consistency with the physical flux is satisfied: $\lim_{\boldsymbol{U}_{i+1}^n \to \boldsymbol{U}_i^n} \boldsymbol{A}_{i+1/2} = \boldsymbol{F}'(\boldsymbol{U}_i^n)$.

According to section 15.3.2 of [18], the Roe matrix may be expressed by the formula

$$\boldsymbol{A}_{i+1/2} = \int_0^1 \boldsymbol{F}'\left(\boldsymbol{U}_i^n + \zeta(\boldsymbol{U}_{i+1}^n - \boldsymbol{U}_i^n)\right) \mathrm{d}\zeta\,, \tag{40}$$

which ensures that the properties 2. and 3. are satisfied. In the case of the system (23), the following $(N+3)\times(N+3)$-matrix is obtained:

$$\boldsymbol{A}_{i+1/2} = \begin{pmatrix} 0 & -1 & 0 & \cdots & 0 & 0 \\ & 0 & -a_1 & \cdots & -a_N & a_{N+1} \\ \vdots & -1 & 0 & \cdots & 0 & 0 \\ & \vdots & \vdots & \vdots & \vdots & \vdots \\ 0 & -1 & 0 & \cdots & 0 & 0 \\ 0 & 0 & 0 & \cdots & 0 & 0 \end{pmatrix}. \tag{41}$$

The coefficients deduced from (40) are for $\ell = 1, \ldots, N$,

$$\begin{aligned} a_\ell &= \frac{(1-g_{i+1}^n)W_\ell'\left((\xi_\ell)_{i+1}^n\right) - (1-g_i^n)W_\ell'\left((\xi_\ell)_i^n\right)}{\rho_0\left((\xi_\ell)_{i+1}^n - (\xi_\ell)_i^n\right)} + (g_{i+1}^n - g_i^n)\frac{W_\ell\left((\xi_\ell)_{i+1}^n\right) - W_\ell\left((\xi_\ell)_i^n\right)}{\rho_0\left((\xi_\ell)_{i+1}^n - (\xi_\ell)_i^n\right)^2}\,, \\ a_{N+1} &= \sum_{\ell=1}^N \frac{W_\ell\left((\xi_\ell)_{i+1}^n\right) - W_\ell\left((\xi_\ell)_i^n\right)}{\rho_0\left((\xi_\ell)_{i+1}^n - (\xi_\ell)_i^n\right)}\,. \end{aligned} \tag{42}$$

To avoid divisions by zero when $(\xi_{\ell^\star})_i^n = (\xi_{\ell^\star})_{i+1}^n$ for some $\ell^\star$ between 1 and N, the coefficients (42) are modified as follows (see Appendix B):

$$\begin{aligned} a_{\ell^\star} &= \left(1 - \frac{g_i^n + g_{i+1}^n}{2}\right)\frac{W_{\ell^\star}''\left((\xi_{\ell^\star})_i^n\right)}{\rho_0}\,, \\ a_{N+1} &= \frac{W_{\ell^\star}'\left((\xi_{\ell^\star})_i^n\right)}{\rho_0} + \sum_{\substack{\ell=1 \\ \ell\neq\ell^\star}}^N \frac{W_\ell\left((\xi_\ell)_{i+1}^n\right) - W_\ell\left((\xi_\ell)_i^n\right)}{\rho_0\left((\xi_\ell)_{i+1}^n - (\xi_\ell)_i^n\right)}\,. \end{aligned} \tag{43}$$

The eigenvalues of $\boldsymbol{A}_{i+1/2}$ are $\{-c_{i+1/2}, 0, \ldots, 0, +c_{i+1/2}\}$, where

$$c_{i+1/2} = \sqrt{\sum_{\ell=1}^N a_\ell}\,. \tag{44}$$

In the Appendix B, we prove that $c_{i+1/2}$ is real in the hyperbolicity domain. Therefore, property 1. is satisfied by $\boldsymbol{A}_{i+1/2}$, and the matrix (41) is a Roe matrix.

3.3. Relaxation part

The relaxation equation (24)-(34) writes as a nonlinear system of first-order differential equations in time:

$$\begin{cases} \dfrac{\partial \xi_\ell}{\partial t} = \dfrac{1}{\eta_\ell}\Big(K_\ell\,(\varepsilon - \xi_\ell) - W'_\ell(\xi_\ell)\Big), \qquad \ell = 1, \dots, N\,, \\ \dfrac{\partial g}{\partial t} = \dfrac{1}{\alpha}\left(\displaystyle\sum_{\ell=1}^{N} W_\ell(\xi_\ell) + \frac{1}{2}K_\ell\,(\varepsilon - \xi_\ell)^2\right) - \dfrac{\phi'(g)}{\alpha}\,, \end{cases} \tag{45}$$

where ε is constant. Due to the various orders of magnitude of the time constants $\tau_{\sigma\ell}$, τ_g in the relaxation spectrum, this differential system is stiff. To avoid stability issues, the operator $\boldsymbol{H}_b$ in (35) is deduced from the adaptive Rosenbrock method of the Odeint C++ library [31]. For the numerical integration of (45) over a duration $\Delta t/2$, the maximum time step of the Rosenbrock method is set to $\Delta t/2$, and the tolerances are 10^{-4} (relative) and 10^{-5} (absolute). Finally, the numerical method (35) is stable under the CFL condition (38). Even if nothing avoids the condition $g < 1$ to be broken numerically, this unwanted event happens only at very high exciting amplitudes.

3.4. Initial conditions and boundary conditions

In the examples of section 4, we assume that the material is initially undeformed and at rest. Hence, the initial data $\boldsymbol{U}(x, 0)$ is zero for all x in the physical domain. To carry out one iteration in time at some grid node i, the numerical values of $\boldsymbol{U}$ at the grid nodes $i-2, \dots, i+2$ are required. Therefore, two "ghost cells" must be added on the left and on the right of the numerical domain, which can account for various types of boundary conditions [18].

- A first case is a piston condition which imposes a particle velocity $\dot{u}_d(t)$ at the abscissa $x = 0$. For compatibility with the initial conditions, one must have $\dot{u}_d(0) = 0$. By construction of the rheological model, the same boundary conditions apply to the variables $\xi_1, \dots, \xi_N$ as to the strain ε. Such a boundary condition is represented numerically by setting for k in $\{1, 2\}$ at each time step

$$\begin{aligned} &\varepsilon^n_{-k} = \varepsilon^n_k\,, \\ &v^n_{-k} = -v^n_k + 2\dot{u}_d(t_{n+1})\,, \\ &(\xi_\ell)^n_{-k} = (\xi_\ell)^n_k\,, \qquad \ell = 1, \dots, N, \\ &g^n_{-k} = g^n_0\,. \end{aligned} \tag{46}$$

- A second case is a free edge at the abscissa $x = L$, which corresponds to a zero-strain condition. Therefore, one has also $\xi_\ell = 0$ for all ℓ at $x = L$. Such a condition is represented by setting for k in $\{1, 2\}$ at each time step

$$\begin{aligned} &\varepsilon^n_{N_x+k} = -\varepsilon^n_{N_x-k}\,, \\ &v^n_{N_x+k} = v^n_{N_x-k}\,, \\ &(\xi_\ell)^n_{N_x+k} = -(\xi_\ell)^n_{N_x-k}\,, \qquad \ell = 1, \dots, N, \\ &g^n_{N_x+k} = g^n_{N_x}\,. \end{aligned} \tag{47}$$

4. Numerical experiments

In this section, several experiments are carried out with the numerical method described in the previous section. The Courant number (38) is set to $\kappa = 0.95$. If not specified differently, the material parameters are given in the tables 1 and A.3. The physical domain is bounded, with length $L = 30$ cm. A particle velocity $\dot{u}_d(t)$ is imposed at the abscissa $x = 0$ using the piston condition (46). A free edge (47) is located at the abscissa $x = L$, as is the case with several experimental setups [4, 5].

4.1. Resonance

Linear viscoelasticity. We consider a linear Zener material ($\beta = 0$, $\delta = 0$, no softening). By definition, the frequency-response function of a linear system is the ratio of the output spectrum ($x = L$) to the input spectrum ($x = 0$), i.e.

$$FRF(\omega) = \frac{\hat{u}(L,\omega)}{\hat{u}_d(\omega)} = \frac{\hat{v}(L,\omega)}{\hat{u}_d(\omega)}\,, \tag{48}$$

where the hat denotes the Fourier transform in time. A Fourier transform in space and time of (22) with $\alpha \to +\infty$ gives the following relation between the wavenumber k and the angular frequency ω,

$$k = \omega\left(\frac{M_{\text{rel}}}{\rho_0}\frac{1}{N}\sum_{\ell=1}^{N}\frac{1+\mathrm{i}\omega\tau_{\varepsilon\ell}}{1+\mathrm{i}\omega\tau_{\sigma\ell}}\right)^{-1/2}\,, \tag{49}$$

where i denotes the imaginary unit. For a harmonic excitation $u_d(t) = \exp(\mathrm{i}\omega t)$, we write the displacement field as a superposition of left-going and right-going monochromatic plane waves. Thus, $u(x,t) = A\exp(\mathrm{i}(\omega t - kx)) + B\exp(\mathrm{i}(\omega t + kx))$, where the wavenumber k satisfies the dispersion relation (49). The coefficients A and B are deduced from the boundary conditions $u(0,t) = u_d(t)$ and $\partial u/\partial x\,(L,t) = 0$. Finally, the ratio of the output to the input (48) at the frequency ω yields

$$FRF(\omega) = \frac{2}{\exp(\mathrm{i}kL) + \exp(-\mathrm{i}kL)}\,, \tag{50}$$

where k is complex and frequency-dependent (49).

To assess the quality of the numerical method, the frequency response is simulated numerically. For this purpose, a broadband chirp signal is used:

$$\dot{u}_d(t) = V\sin\left(2\pi\left(f_{\text{inf}} + \frac{{f_{\text{sup}}}^2 - {f_{\text{inf}}}^2}{4n}t\right)t\right)\mathbf{1}_{0\le t\le 2n/(f_{\text{inf}}+f_{\text{sup}})}\,. \tag{51}$$

Here, the bandwidth is $[f_{\text{inf}}, f_{\text{sup}}] = [1, 15]$ kHz, the velocity amplitude is $V = 0.1$ m/s, and the number of arches is $n = 50$. The numerical solution is computed up to $t = 20$ ms, on a grid with $N_x = 100$ points. During the simulation, the particle velocity at the abscissas $x = 0$ and $x = L$ is recorded (figure 3-(a)). Then, a discrete time-domain Fourier transform of the signals is computed. Figure 3-(b) displays the ratio of the spectra (48) so-obtained. Since the spatial discretization is fine enough — the signals have 43 points per wavelength at the frequency $f_{\text{sup}} = 15$ kHz — the numerical estimation of the frequency response function is very close to the analytical result (50) over the frequency range of the figure. The frequency response is made of resonance peaks, with a quasi-constant quality factor Q (Appendix A). In the viscoelastic case, the resonance frequencies differ slightly from the elastic case, where they are odd multiples of $c/(4L)$.

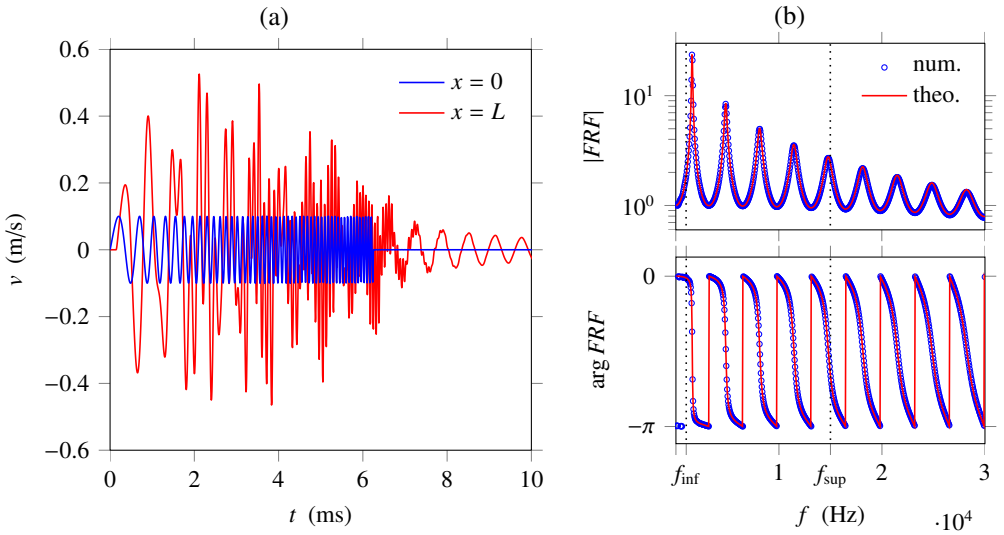

Figure 3: Computation of the frequency response of a linear Zener solid. (a) Time-domain signals at the abscissas $x = 0$ and $x = L$. (b) Numerical estimation (48) of the frequency response compared to the analytical expression (50), modulus (top) and phase (bottom). The vertical dotted lines mark the bandwidth of the exciting signal (51).

Full model. Let us focus on the first mode of vibration which resonance frequency is 1585 Hz. The frequency range of interests reduces to $[f_{\text{inf}}, f_{\text{sup}}] = [1.4, 1.7]$ kHz. In the nonlinear case, defining the frequency response for broadband signals does not make any sense, due to the generation of harmonics. However, one can still define the frequency response for monochromatic signals. To do so, a sine function $\dot{u}_d(t) = V \sin(2\pi f_c t)$ of frequency f_c is used. In the linear case, the value of $FRF(\omega)$ is also given by the ratio

$$FRF(\omega) = \frac{C_1(v(L,t))}{C_1(\dot{u}_d(t))}\,, \tag{52}$$

where C_1 denotes the first complex Fourier coefficient at the angular frequency $\omega = 2\pi f_c$. This definition can still be used in the nonlinear case, where harmonic generation occurs. Since the frequency response is computed at the exciting frequency, the latter must be varied over the range $[f_{\text{inf}}, f_{\text{sup}}]$ to obtain a resonance curve.

For validation purposes, we compute the frequency response of the linear viscoelastic solid from the previous paragraph, but according to the formula (52). The numerical solution is computed on a grid with $N_x = 30$ points, which corresponds to 115 points per wavelength at the frequency f_{sup}. The input velocity amplitude is $V = 0.1$ mm/s. The exciting frequency f_c is increased by $\Delta f_c = (f_{\text{sup}} - f_{\text{inf}})/n$ every 50 ms, which is long enough to consider that the solution has reached the steady state. This increase is performed $n = 19$ times during the simulation. Two receivers record the numerical solution at the abscissas $x = 0$ and $x = L$. The Fourier coefficients C_1 are computed by numerical integration over the last period of signal at each exciting frequency f_c. To do so, the velocity signals are interpolated by a cubic spline over their last period, and the midpoint rule is used for numerical integration. As illustrated in figure 4-(a), a high number of points per wavelength is required to compute accurately the frequency response in the vicinity of the resonance peak, where the modulus is slightly underestimated. This issue is due

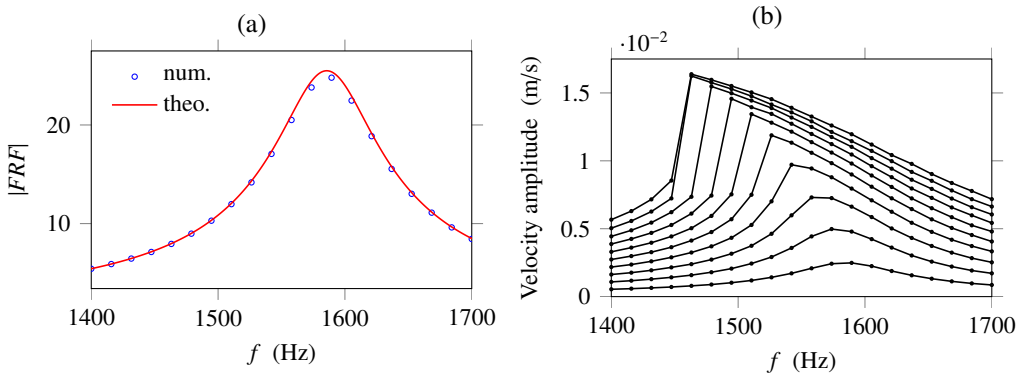

Figure 4: Computation of the frequency response (52) of nonlinear solids. (a) Validation on a linear viscoelastic material, by comparison with the analytical expression (50). (b) Numerical estimation of the output velocity amplitude ($x = L$) in the nonlinear case for increasing exciting amplitudes.

to the amplification of numerical errors near the resonance, and to the duration of the simulation until the steady-state is reached.

Now, the full model is considered. The forcing amplitude V is ranging from 0.1 mm/s to 1 mm/s by steps of 0.1 mm/s, and the exciting frequency is increased by Δf_c every 100 ms. Figure 4-(b) displays the frequency-evolution of the output velocity amplitude $2\,|C_1(v(L,t))|$. According to (52), this quantity is equal to $V\,|FRF(\omega)|$ in the linear case. In the present nonlinear case, the velocity amplitude is not proportional to V anymore. In particular, one can note the frequency-shift of resonance peaks towards lower frequencies as V increases. At low values of V, the linear frequency response from figure 4-(a) is recovered. At high values of V, one can note the occurrence of a jump in the resonance curve. These features are typical of the experimental observations made on rock samples [2, 3].

4.2. Dynamic acoustoelasticity

In dynamic acousto-elastic testing, the setup is similar. The parameters of the discretization are the same as in the previous case. A resonance frequency is chosen, so as to maximize the strain levels. The sinusoidal source with frequency $f_c = 1585$ Hz and velocity amplitude V is turned on from $t = 0$ to $t \approx 50.4$ ms. Now, the receiver records the numerical solution at the abscissa $x = 0.1$ m, up to $t = 80$ ms.

Figure 5-(a) displays the effective elastic modulus $\rho_0\, c^2$ (25), which is recorded at the position of the receiver. A slow decrease of the elastic modulus combined with fast oscillations is observed. The frequency of the fast oscillations is the frequency f_c of the source signal. When the source is stopped ($t \approx 50.4$ ms), the amplitude of the fast oscillations diminishes, and the elastic modulus recovers gradually its initial value. The duration of the softening is related to the characteristic time τ_g of the slow dynamics (21), and to the quality factor Q. As observed experimentally, the softening phenomenon is accentuated when the amplitude of forcing V is increased.

Figure 5-(b) focuses on the steady-state solution. Here, the last period of signal before the end of excitation is used. When the effective elastic modulus is represented with respect to the strain at the position of the receiver, a hysteresis curve is obtained. The shape of the hysteresis

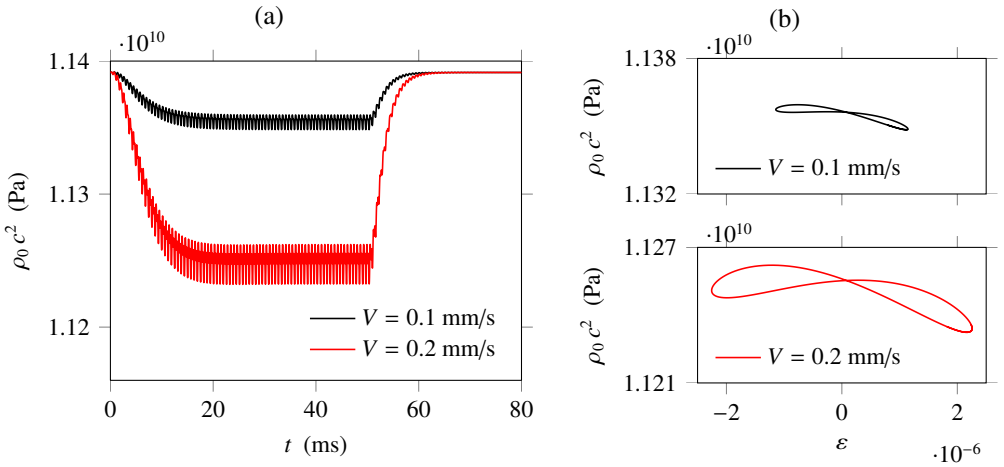

Figure 5: Dynamic acousto-elasticity. (a) Softening of the material, as recorded by the receiver at the abscissa $x = 0.1$ m. (b) Hysteresis curves in steady-state ($t \approx 50$ ms).

curve is related to the coefficients β and δ of the polynomial law (4), and to the dissipation in the material (see figure 2 and [14]).

5. Conclusion

A one-dimensional model of continuum which includes nonlinear elasticity, viscoelastic attenuation and softening is proposed. This model is thermodynamically well posed, and reproduces the main experimental features qualitatively. A numerical method based on finite volumes is introduced, so as to solve the equations of motion efficiently. Resonance experiments and dynamic acousto-elasticity experiments are simulated, and qualitative agreement with experimental results is obtained in both cases.

Experimental validations are currently carried out, in order to estimate the value of the parameters of the model. The expressions of the evolution equation (19) and of the storage energy (15) are not unique, and may be a key for fine tuning of the model. The use of the harmonic balance method for the computation of resonance curves is currently explored. Future work will be devoted to 2D and 3D numerical modeling, in particular to propose a more realistic framework for the numerical simulation of DAET experiments.

6. Acknowledgments

This work was supported by the interdisciplinary mission of CNRS (Inphyniti). It was also done in the framework of Labex MEC (ANR-10-LABX-0092) funded by the French National Research Agency (ANR), and of the DCND project funded by the French National Radioactive Waste Management Agency (ANDRA).

Appendix A. Parameters of the viscoelastic model

Let us consider the case of linear Zener material, which dispersion relation is given by (49). If the phase velocity $\omega/\mathrm{Re}\, k$ is equal to $c_{\mathrm{ref}} = \sqrt{M_0/\rho_0}$ at a given angular frequency ω_{ref}, then

Table A.3: Optimized coefficients of the Zener model.

ℓ	$\tau_{\sigma\ell}$ (ms)	$\tau_{\varepsilon\ell}$ (ms)
1	$2.39556647121688 \times 10^{-1}$	$3.26820245620307 \times 10^{-1}$
2	$5.22532018808709 \times 10^{-2}$	$6.37792234728574 \times 10^{-2}$
3	$1.53966793063646 \times 10^{-2}$	$1.87515784083158 \times 10^{-2}$
4	$4.54569618004597 \times 10^{-3}$	$5.62759706637171 \times 10^{-3}$
5	$9.68524210724988 \times 10^{-4}$	$1.40683422528016 \times 10^{-4}$

the relaxed elastic modulus

$$M_{\text{rel}} = M_0 \,\text{Re}\left(\left(\frac{1}{N}\sum_{\ell=1}^{N}\frac{1+\text{i}\omega_{\text{ref}}\tau_{\varepsilon\ell}}{1+\text{i}\omega_{\text{ref}}\tau_{\sigma\ell}}\right)^{-1/2}\right)^2 \tag{A.1}$$

is deduced from the expression of the wavenumber k at the angular frequency ω_{ref}. The reciprocal of the quality factor is given by [10, 20]

$$Q^{-1} = \omega\left(\sum_{\ell=1}^{N}\frac{\tau_{\varepsilon\ell}-\tau_{\sigma\ell}}{1+\omega^2{\tau_{\sigma\ell}}^2}\right)\Bigg/\left(\sum_{\ell=1}^{N}\frac{1+\omega^2\tau_{\varepsilon\ell}\tau_{\sigma\ell}}{1+\omega^2{\tau_{\sigma\ell}}^2}\right). \tag{A.2}$$

The method to obtain the coefficients $\tau_{\sigma\ell}$, $\tau_{\varepsilon\ell}$ is described hereinafter.

One can note that the quality factor of the Zener model (A.2) depends only on the angular frequency ω, the number of relaxation mechanisms N, and the relaxation times $\tau_{\sigma\ell}$, $\tau_{\varepsilon\ell}$. If a reference frequency-dependent quality factor is known and a number N of relaxation mechanisms is chosen, then the distance between the quality factor in (A.2) and the reference quality factor can be minimized with respect to the parameters $\tau_{\sigma\ell}$, $\tau_{\varepsilon\ell}$. In practice, the distance is minimized over a set of $4N$ frequencies, which are logarithmically distributed over a frequency range of interest $[f_{\text{min}}, f_{\text{max}}]$. Optimization constraints are imposed to ensure that $\tau_{\varepsilon\ell} > \tau_{\sigma\ell} > 0$, which is necessary for positive spring and dashpot constants

$$M_\ell = \frac{\tau_{\varepsilon\ell}}{\tau_{\sigma\ell}}\frac{M_{\text{rel}}}{N}\,, \qquad K_\ell = \frac{\tau_{\varepsilon\ell}}{\tau_{\varepsilon\ell}-\tau_{\sigma\ell}}\frac{M_{\text{rel}}}{N}\,, \qquad \eta_\ell = \frac{{\tau_{\varepsilon\ell}}^2}{\tau_{\varepsilon\ell}-\tau_{\sigma\ell}}\frac{M_{\text{rel}}}{N} \tag{A.3}$$

in the rheological model (figure 1). If the relaxation times $\tau_{\sigma\ell}$ are sorted in descending order, then the constraint $1/\tau_{\sigma N} < f_{\text{max}}$ is added to the optimization procedure. The reader is referred to [22] for details about such an optimization.

The frequency evolution of the quality factor's inverse Q^{-1} so-obtained is represented in figure A.6-(b), where a constant reference quality factor $Q = 20$ is chosen, and $N = 5$ Zener mechanisms are considered. The corresponding optimized coefficients are given in table A.3. In the figure A.6-(b), the reference quality factor is reached by the optimized Zener model over the frequency range $[1, 100]$ kHz of the optimization procedure. The frequency evolution of the phase velocity $\omega/\text{Re}\,k$ deduced from the dispersion relation (49) is represented in figure A.6-(a) as well as the attenuation $-\text{Im}\,k$. It can be verified that the phase velocity is equal to c_{ref} at the angular frequency ω_{ref}.

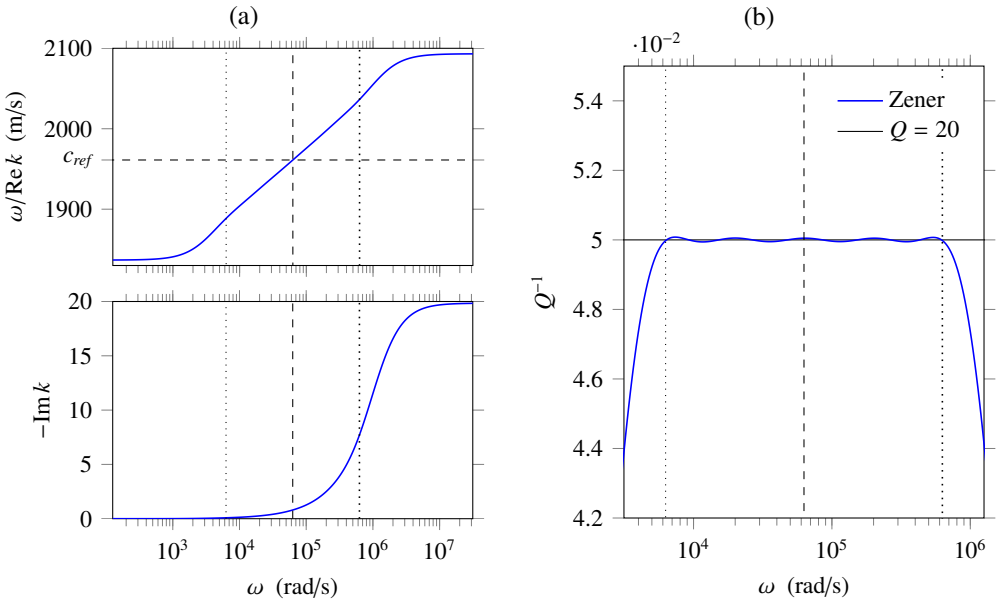

Figure A.6: (a) Phase velocity (top) and attenuation (bottom) of the generalized Zener model, as a function of the angular frequency. (b) Quality factor of the generalized Zener model (A.2) compared to the reference $Q = 20$. The vertical dashed line marks $\omega_{\mathrm{ref}} = 2\pi \times 10^4$ rad/s, whereas the vertical dotted lines mark the bounds $2\pi f_{\min} = 0.1\,\omega_{\mathrm{ref}}$ and $2\pi f_{\max} = 10\,\omega_{\mathrm{ref}}$ of the frequency range of optimization.

Appendix B. Spectrum of the matrix $A_{i+1/2}$ in (41)

The eigenvalues of the matrix $\boldsymbol{A}_{i+1/2}$ are $\{-c_{i+1/2}, 0, \dots, 0, +c_{i+1/2}\}$, where $c_{i+1/2}$ is given in (44). In order to show that $c_{i+1/2}$ is real, one must show that the sum of the coefficients $(a_\ell)_{1\le\ell\le N}$ is positive. The proof is based on the fact that the variables $\xi_1, \dots, \xi_N$ and g satisfy the hyperbolicity condition, i.e. the strain energy $\xi_\ell \mapsto W_\ell(\xi_\ell)$ is restricted to a domain where it is convex, and g is bounded by 1 (cf. section 2.3).

If $(\xi_{\ell^\star})_i^n = (\xi_{\ell^\star})_{i+1}^n$ for some $\ell^\star$ between 1 and N, then the convexity of $W_{\ell^\star}$ and the bound $g < 1$ imply that $a_{\ell^\star}$ is positive (43). Otherwise, the coefficient a_ℓ in (42) is rewritten as

$$
\begin{aligned}
a_\ell = {} & \frac{W_\ell'\left((\xi_\ell)_{i+1}^n\right) - W_\ell'\left((\xi_\ell)_i^n\right)}{\rho_0\left((\xi_\ell)_{i+1}^n - (\xi_\ell)_i^n\right)} \\
& - g_i^n \frac{W_\ell\left((\xi_\ell)_{i+1}^n\right) - W_\ell\left((\xi_\ell)_i^n\right) - W_\ell'\left((\xi_\ell)_i^n\right)\left((\xi_\ell)_{i+1}^n - (\xi_\ell)_i^n\right)}{\rho_0\left((\xi_\ell)_{i+1}^n - (\xi_\ell)_i^n\right)^2} \\
& - g_{i+1}^n \frac{W_\ell\left((\xi_\ell)_i^n\right) - W_\ell\left((\xi_\ell)_{i+1}^n\right) - W_\ell'\left((\xi_\ell)_{i+1}^n\right)\left((\xi_\ell)_i^n - (\xi_\ell)_{i+1}^n\right)}{\rho_0\left((\xi_\ell)_{i+1}^n - (\xi_\ell)_i^n\right)^2}.
\end{aligned}
\tag{B.1}
$$

Due to the convexity of W_ℓ, the first right-hand side term is positive, as well as the ratios multi-

plied by $-g_i^n$ and $-g_{i+1}^n$. The bound $g < 1$ implies

$$
\begin{aligned}
a_\ell \geq & \frac{W'_\ell\left((\xi_\ell)_{i+1}^n\right) - W'_\ell\left((\xi_\ell)_i^n\right)}{\rho_0\left((\xi_\ell)_{i+1}^n - (\xi_\ell)_i^n\right)} \\
& - \frac{W_\ell\left((\xi_\ell)_{i+1}^n\right) - W_\ell\left((\xi_\ell)_i^n\right) - W'_\ell\left((\xi_\ell)_i^n\right)\left((\xi_\ell)_{i+1}^n - (\xi_\ell)_i^n\right)}{\rho_0\left((\xi_\ell)_{i+1}^n - (\xi_\ell)_i^n\right)^2} \\
& - \frac{W_\ell\left((\xi_\ell)_i^n\right) - W_\ell\left((\xi_\ell)_{i+1}^n\right) - W'_\ell\left((\xi_\ell)_{i+1}^n\right)\left((\xi_\ell)_i^n - (\xi_\ell)_{i+1}^n\right)}{\rho_0\left((\xi_\ell)_{i+1}^n - (\xi_\ell)_i^n\right)^2},
\end{aligned}
\tag{B.2}
$$

and hence, $a_\ell \geq 0$. This ends the proof: $\boldsymbol{A}_{i+1/2}$ is a Roe matrix. Equation (B.1) is also useful to obtain (43) by taking the limit as $(\xi_\ell)_{i+1}^n \to (\xi_\ell)_i^n$.

References

[1] R. A. Guyer, P. A. Johnson: Nonlinear mesoscopic elasticity: evidence for a new class of materials. Phys. Today **52** (1999) 30–36.

[2] J. A. TenCate: Slow dynamics of earth materials: an experimental overview. Pure Appl. Geophys. **168** (2011) 2211–2219.

[3] P. A. Johnson, B. Zinszner, P. N. J. Rasolofosaon: Resonance and elastic nonlinear phenomena in rock. J. Geophys. Res. **101** (1996) 11 553–11 564.

[4] G. Renaud, P.-Y. Le Bas, P. A. Johnson: Revealing highly complex elastic nonlinear (anelastic) behavior of Earth materials applying a new probe: Dynamic acoustoelastic testing. J. Geophys. Res.-Sol. Ea. **117** (2012) B06202.

[5] J. Rivière, G. Renaud, R. A. Guyer, P. A. Johnson: Pump and probe waves in dynamic acoustoelasticity: comprehensive description and comparison with nonlinear elastic theories. J. Appl. Phys. **114**-5 (2013) 054905.

[6] T. Meurer, J. Qu, L. J. Jacobs. Wave propagation in nonlinear and hysteretic media—a numerical study. Int. J. Solids Struct. **39**-21 (2002) 5585–5614.

[7] Y. Li, O. Bou Matar, B. Li, X. Chen. Pseudo-spectral simulation of 1D nonlinear propagation in heterogeneous elastic media. Wave Motion **52** (2015) 54–65.

[8] V. E. Nazarov, A. V. Radostin, L. A. Ostrovsky, I. A. Soustova. Wave Processes in Media with Hysteretic Nonlinearity. Part I. Acoustical Physics **49**-3 (2003) 405–415.

[9] O. O. Vakhnenko, V. O. Vakhnenko, T. J. Shankland, J. A. Ten Cate: Strain-induced kinetics of intergrain defects as the mechanism of slow dynamics in the nonlinear resonant response of humid sandstone bars. Phys. Rev. E **70** (2004) 015602.

[10] N. Favrie, B. Lombard, C. Payan: Fast and slow dynamics in a nonlinear elastic bar excited by longitudinal vibrations. Wave Motion **56** (2015) 221–238.

[11] V. Lyakhovsky, Y. Ben-Zion, A. Agnon: Distributed damage, faulting, and friction. J. Geophys. Res.-Sol. Ea. **102**-B12 (1997) 27635–27649.

[12] V. Lyakhovsky, Z. Reches, R. Weinberger, T. E. Scott: Non-linear elastic behaviour of damaged rocks. Geophys. J. Int. **130**-1 (1997) 157–166.

[13] V. Lyakhovsky, Y. Hamiel, J.-P. Ampuero, Y. Ben-Zion: Non-linear damage rheology and wave resonance in rocks. Geophys. J. Int. **178**-2 (2009) 910–920.

[14] H. Berjamin, N. Favrie, B. Lombard, G. Chiavassa: Nonlinear waves in solids with slow dynamics: an internal-variable model. Proc. R. Soc. A **473** (2017) 20170024.

[15] G. A. Maugin, W. Muschik: Thermodynamics with internal variables. Part I. General concepts. J. Non-Equilib. Thermodyn. **19** (1994) 217–249.

[16] G. A. Maugin: The saga of internal variables of state in continuum thermomechanics (1893–2013). Mech. Res. Commun. **69** (2015) 79–86.

[17] E. Godlewski, P.-A. Raviart. Numerical Approximation of Hyperbolic Systems of Conservation Laws. Springer, 1996.

[18] R. J. LeVeque. Finite-Volume Methods for Hyperbolic Problems. Cambridge University Press, 2002.

[19] R. Velasco-Segura, P. L. Rendón: A finite volume approach for the simulation of nonlinear dissipative acoustic wave propagation. Wave Motion **58** (2015) 180–195.
[20] J. M. Carcione: Wave Fields in Real Media: Wave Propagation in Anisotropic, Anelastic, Porous and Porous Media. Elsevier, Oxford, 2001.
[21] P. Moczo, J. Kristek: On the rheological models used for time-domain methods of seismic wave propagation. Geophys. Res. Lett. **32**-1 (2005) L01306.
[22] E. Blanc, D. Komatitsch, E. Chaljub, B. Lombard, Z. Xie: Highly accurate stability-preserving optimization of the Zener viscoelastic model, with application to wave propagation in the presence of strong attenuation. Geophys. J. Int. **205**-1 (2016) 427–439.
[23] R. W. Ogden, F. G. Roxburgh: A pseudo-elastic model for the Mullins effect in filled rubber. Proc. R. Soc. A **455** (1999) 2861–2877.
[24] G. A. Holzapfel: Nonlinear Solid Mechanics: A Continuum Approach for Engineering. John Wiley & Sons, 2000.
[25] C. M. Dafermos. Hyperbolic Conservation Laws in Continuum Physics, 2nd ed. Springer, 2005.
[26] H. Berjamin, B. Lombard, G. Chiavassa, N. Favrie: Analytical solution to 1D nonlinear elastodynamics with general constitutive laws. Wave Motion **74** (2017) 35–55.
[27] C.-W. Shu: High order weighted essentially nonoscillatory schemes for convection dominated problems. SIAM Rev. **51**-1 (2009) 82126.
[28] T. Schwartzkopff, M. Dumbser, C.-D. Munz: Fast high order ADER schemes for linear hyperbolic equations. J. Comput. Phys. **197**-2 (2004) 532–539.
[29] T. Schwartzkopff, M. Dumbser, C.-D. Munz: Arbitrary high order finite volume schemes for linear wave propagation. Computational Science and High Performance Computing II (2006) 129–144.
[30] R. J. LeVeque: Numerical Methods for Conservation Laws, 2nd ed. Birkhäuser, 1992.
[31] K. Ahnert, M. Mulansky: Odeint – Solving Ordinary Differential Equations in C++. AIP Conf. Proc. **1389** (2011) 1586–1589.